Topography Correction for Airborne Synthetic Aperture Radar

Ahmed Azouz, PhD
Egyptian Armed Forces

Abstract: Airborne synthetic aperture radar (SAR) is an essential tool for modern remote sensing applications. The motion compensation (MOCO) in SAR processing is usually carried out by assuming a reference level to compute the range displacements and phase corrections to apply to each received echo. This means that phase histories of targets at heights different from the reference level cannot be matched accurately, which might yield several effects in the final compressed image. Topography correction for airborne SAR accommodates topography variations during SAR data processing, using an external digital elevation model (DEM). The aperture-dependent MOCO is compensation the phase error of all targets before azimuth compression, resulting in an enhanced image quality. In this paper, analysis the effect of topography variations in focused image (after range and azimuth compression). Then presented an efficient way to use the information given by an external DEM to take into account the motion of the aircraft along the whole synthetic aperture is presented. Finally, real simulated-data experiments show that the proposed approach is appropriate for highly precise imaging of airborne SAR.

Keywords: Airborne synthetic aperture radar, Motion Compensation, aperture-dependent MOCO.

1-Introduction

Synthetic aperture radar (SAR) is a remote sensing system to generate high-resolution microwave images of the observed scene. It is mounted on-board a platform, such as aircraft, satellite or unmanned aerial vehicle (UAV), which is supposed to fly at a constant velocity along a nominal trajectory. For SAR systems, motion is a solution as well as a problem. The problem arises from trajectory deviations and instability of the platform velocities, which not only cause serious image blurring, but also geometric distortion of the SAR imagery. The motion errors can be obtained from the synchronous measurements of navigation systems, and motion compensation (MOCO) is then performed subsequently. The navigation measurements usually provide only coarse MOCO, such as removal of the non-systematic range cell migration (NRCM) and partial phase errors [1-4]. Autofocus approaches are subsequently applied to estimate the residual motion errors. A method presented in [5] is based on the combination of range alignment and phase gradient autofocus (PGA) [6]: the NRCM is corrected by the range alignment techniques with the inertial navigation system (INS) measurements, and the phase error is estimated by PGA. In the raw-data-based approaches, autofocus techniques are employed to estimate motion errors adaptively. PGA is one of the most popular autofocus algorithms. Recent improvements in the PGA algorithms, including the quality PGA (QPGA) and the weighted phase estimation by the weighted PGA (WPGA), are presented in [7, 8], respectively. The NRCM MOCO strategy suffices for a flat terrain and for resolutions in the order of 1 m [9]. While the topographic variation within the observed scene and azimuth dependence of the motion error are considered, a new MOCO strategy, referred to as precise topography- and aperture-dependent MOCO, is proposed in [9-11].

In this paper, we analyzed the effect of topography variations of illuminated area in focused image. That we get after range and azimuth compression. Then explain proposal method aperture-dependent MOCO for topography correction that applied after second order MOCO and before azimuth compression.

We organize this paper as follows. In Section 2, the error duo to topography variations derived that affected on focused image. Then, Section 3 used the aperture-dependent MOCO is compensation the phase error of all targets before azimuth compression. In Section 4, the simulated data is used to validate the proposed method. Finally, conclusions are drawn in Section 5.

2. Effect of topography variations on focused image

The Airborne-SAR data acquisition geometry is shown in Fig. 1, where the linear straight line (Y-axis) denotes the nominal track, and the curve represents the real or actual track. In the ideal case, the antenna phase center (APC) of the radar moves along the nominal path at a constant velocity V. However, owing to the displacement of the real track from the nominal one, additional range error from radar to target arises. Assume that the pulse repetition interval is T_r. APCs are located at a constant interval of $V T_r$ along the Y-axis direction with a reference height of H. The actual and ideal APC positions at the slow time t_a are $[X(t_a), Y(t_a), Z(t_a)]$ and $[0, V t_a, H]$, respectively. The motion error vector, defined as the displacement between the actual and nominal paths, is $d(t_a) = [\Delta x(t_a), Y(t_a) - V t_a, \Delta z(t_a)]$ where $\Delta x(t_a)$ and $\Delta z(t_a)$ denote the motion displacements in the normal plane, i.e., the cross-track motion errors. The position of the illuminating antenna is now completely described by the azimuth coordinate $y' = V t_a$ and by the vector $d(t_a)$, the platform displacements from the nominal track. The correction is made assuming a constant reference height plan at z_o, which is the reference plan. Considering a scatter point at $P(x, y, z)$ and in the unsquinted observation mode (broadside), the position of that point in reference plan is $P_o(x_o, y_o, z_o)$. Then, the instantaneous range from the nominal APC position y' to the scatter P_o is:

$$R_n(t_a; r, y) = \sqrt{x_o^2 + (y' - y_o)^2 + [z_o - H]^2} = \sqrt{(y' - y_o)^2 + r^2}$$
$$= \sqrt{(V t_a - y_o)^2 + r^2} = r + \Delta R(t_a; r, y_o) \tag{1}$$

where $r = \sqrt{x_o^2 + (z_o - H)^2}$ is the distance of the closest approach with respect to the nominal track.

The instantaneous range from the actual APC position A to the scatter P is

$$R(t_a; r, y) = \sqrt{(x - \Delta x)^2 + [y - (y' + \Delta y)]^2 + [\{(z_o + \Delta h) - H\} - \Delta z]^2}$$
$$= \sqrt{[(x_o + x_{\Delta h}) - \Delta x]^2 + [(y_o + y_{\Delta h}) - (y' + \Delta y)]^2 + [\{(z_o + \Delta h) - H\} - \Delta z]^2} \tag{2}$$
$$= R_n(t_a; r, y) + \delta R(t_a; r, y)$$

where $\delta R(t_a; r, y)$ is the slant range error, Δh is the difference between actual height and reference high tog scattered, and $x_{\Delta h}$ is the shift in X-axis due to topography variation, and

$y_{\Delta h}$ is the shift in Y-axis due to topography variation. The slant range error can be approximately as follows:

$$\delta R\left(t_a; r, y\right) = R\left(t_a; r, y\right) - R_n\left(t_a; r, y\right)$$

$$\approx \frac{\left(Vt_a - y_o\right)}{R_n\left(t_a; r, y\right)}\Delta y(t_a) - \frac{x_o}{R_n\left(t_a; r, y\right)}\Delta x(t_a) - \frac{\left(z_o - H\right)}{R_n\left(t_a; r, y\right)}\Delta z(t_a)$$

$$+ \frac{\Delta x(t_a)^2 + \Delta z(t_a)^2 + \Delta y(t_a)^2}{2R_n\left(t_a; r, y\right)} + \frac{\left(x_o - \Delta x\right)x_{\Delta h}}{R_n\left(t_a; r, y\right)} - \frac{\left(\left(y' - y_o\right) + \Delta y\right)y_{\Delta h}}{R_n\left(t_a; r, y\right)} \qquad (3)$$

$$+ \frac{\left[\left(z_o - H\right) - \Delta z(t_a)\right]\Delta h}{R_n\left(t_a; r, y\right)} + \frac{x_{\Delta h}^2 + y_{\Delta h}^2 + \Delta h^2}{2R_n\left(t_a; r, y\right)}$$
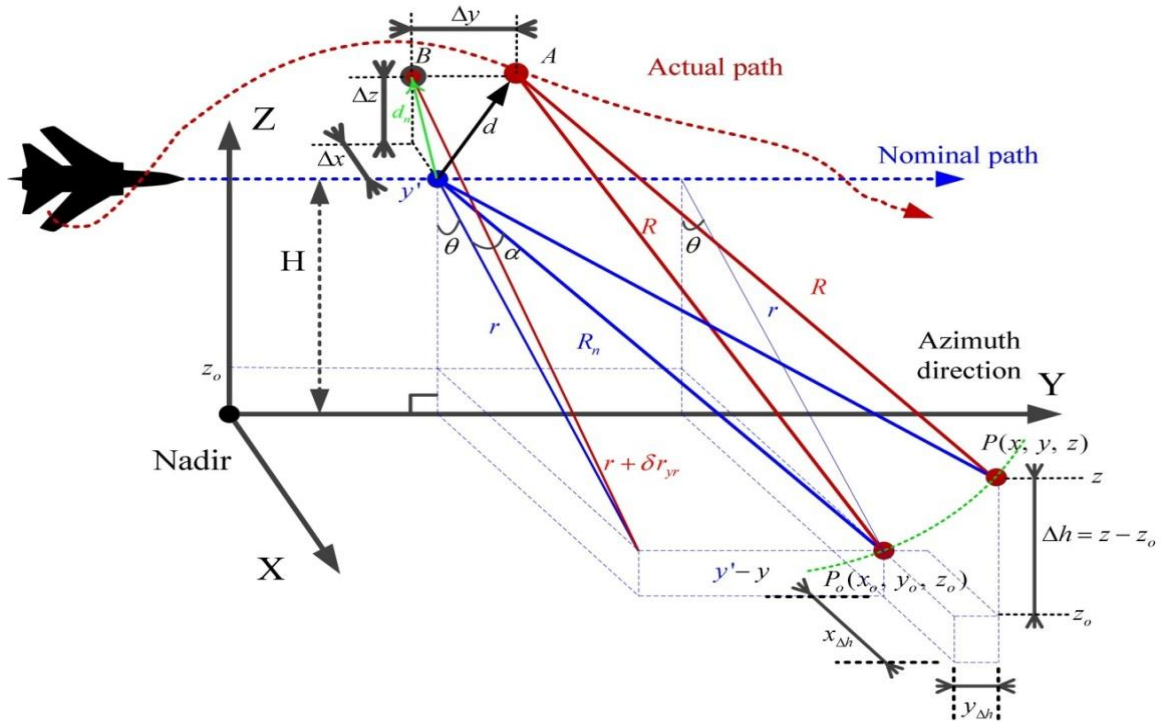

Fig. 1 SAR system geometry in the presence of trajectory deviation and topography Variations.

Let θ denote the off-nadir angle, i.e., the look angle associated with the scatterer P, and α is the instantaneous squint angle as a function of azimuth position. That can be written as following:

$$\sin \alpha = \frac{\left(V t_a - y\right)}{R_n\left(t_a; r, x\right)} \ , \ \cos \alpha = \frac{r}{R_n\left(t_a; r, x\right)} \ , \ \sin \theta = \frac{x}{r} \ , \ and \ \cos \theta = \frac{\left(z_o - H\right)}{r} \qquad (4)$$

$$-\theta_a / 2 < \alpha < \theta_a / 2$$

where θ_a is the azimuth beamwidth. Substituting Eq. (4) into Eq. (3), and ignoring the higher order terms, the range displacement can be approximated as

$$\delta R\left(t_a; r, x\right) \approx \sin\alpha\,\Delta y - \cos\alpha\left(\sin\theta\,\Delta x + \cos\theta\,\Delta z\right)$$
$$+\left[\cos\alpha\,\sin\theta\right]x_{\Delta h} - \left[\sin\alpha\right]y_{\Delta h} + \left[\cos\alpha\,\cos\theta\right]\Delta h \qquad (5)$$
$$= \delta R_{ref}\left(t_a; r, x\right) + \delta R_{topo}\left(t_a; r, x\right)$$

where $\delta R_{ref}\left(t_a; r, x\right)$ and $\delta R_{topo}\left(t_a; r, x\right)$ are range error related to reference plane and topographic variation are shown in Eq. (6) and Eq. (7), respectively.

$$\delta R_{ref}\left(t_a; r, x\right) = \sin\alpha\,\Delta y - \cos\alpha\left(\sin\theta\,\Delta x + \cos\theta\,\Delta z\right) \qquad (6)$$

$$\delta R_{topo}\left(t_a; r, x\right) = -\sin\alpha\,y_{\Delta h} + \cos\alpha\left(\sin\theta\,x_{\Delta h} + \cos\theta\,\Delta h\right) \qquad (7)$$

In Eq. (6) and Eq. (7) the first terms in are caused by the along-track motion error and the second terms are the cross-track error, and the last four terms is the effect of topographic variation. Assuming that range compression and range cell migration correction (RCMC) have been applied, the signal in time domain for a given target has the following expression in the unsquinted observation mode (broadside):

$$s\left(t_a, t; r\right) = A_o \exp\left[-j\frac{4\pi}{\lambda}\sqrt{r^2 + V^2\left(t_a - t_{ao}\right)^2}\right] \times \exp\left[-j\frac{4\pi}{\lambda}\varepsilon\left(t_a, r\right)\right]$$
$$\times s_a\left(t_a - t_{ao}\right) \times s_{rc}\left(t - \frac{2r}{c}\right) \qquad (8)$$

where A_o is a complex constant, t_a is the azimuth time, t is the range time, r is the closest approach distance, V is the forward velocity of the platform, t_{ao} is the zero-Doppler time position, c is the speed of light, $\varepsilon(t_a, r)$ is the uncompensated trajectory for that target, $s_{rc}(\cdot)$ is the range compressed envelopes, and $s_a(\cdot)$ is the azimuth compressed envelopes.

In chirp scaling algorithms, a two-step MOCO is commonly applied [12], where first-order MOCO compensation both envelope and phase for a reference range and height, while second-order MOCO corrects for each range after RCMC and range compression. Therefore, second-order MOCO is carried out multiplying Eq. (8) by a complex function containing the residual range-dependent correction $\varepsilon_{z_0}\left(t_a, r\right)$, where subscript z_0 means the correction is made assuming a constant reference height. If the introduced term is equal to the error $\varepsilon(t_a, r)$, MOCO is applied correctly, i.e., the height of the target is equal to the reference one used during second-order MOCO. However, this is normally not the case if strong topography variations are present in the scene. Therefore, a phase error remains along the phase history of the target, which, after azimuth compression, yields to phase errors and both degradation and displacement of the impulse response along azimuth direction. Consequently, although conventional MOCO has been applied, the error depends on the topography, making azimuth compression still space-variant. The main problem to overcome is the fact that for a given pulse, it is not possible to correct for more than one height. The subaperture approach presented in Section 3 expounds a solution to this problem.

The phase offset value due to second-order MOCO mismatch can be evaluated analytically for the maximum of the impulse response. Assuming time domain azimuth compression, i.e., a cross-correlation, the expression for instant t_{ao} is

$$s_c\left(t_{ao},t;r\right) = A\exp\left[-j\frac{4\pi}{\lambda}r\right]s_{rc}\left(t-\frac{2r}{c}\right)\times \int_{L_{SAR}} s_a\left(\tau-t_{ao}\right)$$

$$\exp\left[-j\frac{4\pi}{\lambda}\varepsilon\left(\tau,r\right)\right]\exp\left[-j\frac{4\pi}{\lambda}\varepsilon_{z_0}\left(\tau,r\right)\right]d\tau \qquad (9)$$

where L_{SAR} is the length of the synthetic aperture in seconds. The integral in Eq. (9) should have a zero phase value.

With the use of an external DEM, one could think of computing the integral in Eq. (9) for each pixel of the image, and correct the phase. The next section expounds a solution that avoids all harmful effects by modifying the phase history of targets accurately before azimuth compression.

3. Topography-Dependent Motion Compensation with Subaperture

Topography-dependent motion compensation started after conventional second-order MOCO using the height information of an external DEM. This solution has the drawback that the correction is only applied at one referable height, which could be the mean height of the antenna footprint for that pulse, and which is not able to accommodate for other heights. The system parameters are listed in Table 1 and a synthetic aperture of ~350 m in midrange. If the observed scene had strong topography variations, the correction would be insufficient.

Table 1 Airborne-SAR Sensor Parameters

Nominal height (H)	12000 m	Chirp duration (T_p)	50 μs
Midrange coordinate (R_o)	18275 m	Chirp bandwidth (B_r)	180 MHz
Wavelength (λ)	1.875 cm	Range pixel dimension ($R_s = c/2/f_s$)	50 cm
Platform velocity (V)	208 m/s	Azimuth pixel dimension ($A_s = V/PRF$)	20.8 cm
Sampling Frequency (f_s)	300 MHz	Pulse Repetition Frequency (PRF)	1000 Hz

The algorithm proposed in this section allows for an angle-accommodation to follow a similar principle than the one presented in [13-15]. The distinction between targets in azimuth by Doppler beam sharpening (DBS) are shown in Fig. 2.
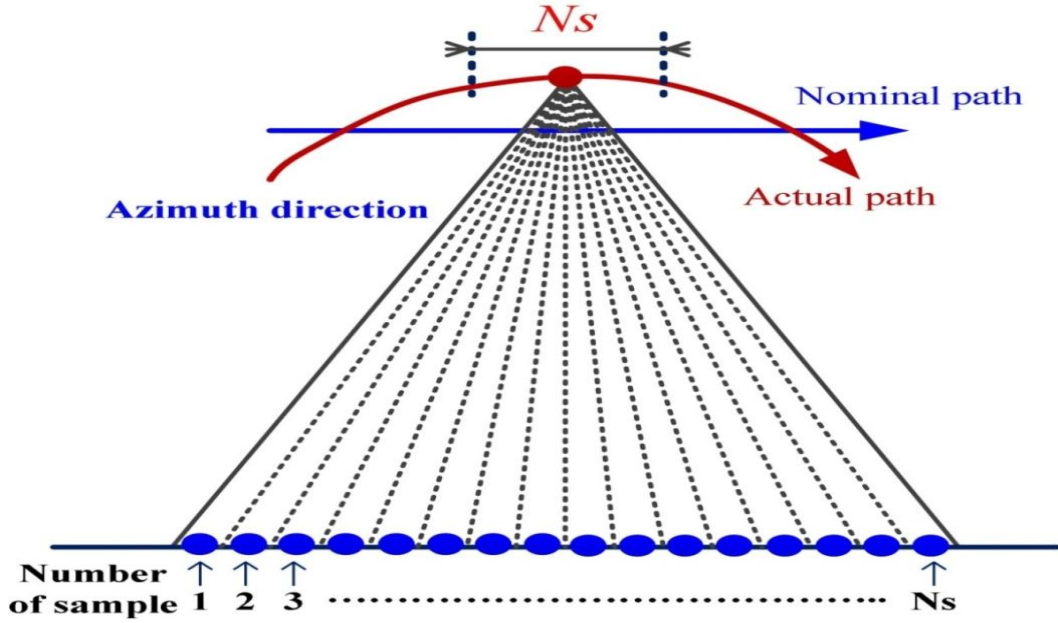
Fig. 2 Separation targets in azimuth by Doppler beam sharpening (DBS).

The max number of samples Ns depends on the concept of Doppler Beam Sharpening (DBS). DBS technique takes the azimuth fast Fourier transform process to construct DBS sub-images right after range pulse compression. Fig. 2 shows the geometric relationship between the point target and airborne-SAR in slant range plane. In Fig. 2, airborne-SAR makes a uniform rectilinear path along the Y-axis with the velocity V, P is the scatter point target, and α is the instantaneous squint angle as a function of azimuth position. The slant ranges of point target is r and $r + \Delta r$ corresponding to the positions of the airborne-SAR A_1 and A_2 respectively. The echo of a point target of P in Fig. 2 can be obtained as follows:

$$
\begin{aligned}
s_A(t_a, r) &= \exp\left[-j\frac{4\pi}{\lambda}\left(\sqrt{r^2 + V^2 t_a^2 - 2rV t_a \cos\left(\frac{\pi}{2}-\alpha\right)}\right)\right] \\
&\approx \exp\left[-j\frac{4\pi}{\lambda}\left(r - V t_a \sin(\alpha) + \frac{V^2 t_a^2 \cos^2(\alpha)}{2r}\right)\right] \quad t_a \in \left[-\frac{T_c}{2}, \frac{T_c}{2}\right]
\end{aligned}
\tag{10}
$$

where T_c is the integration time in the azimuth direction. To realize the coherent summation, the following inequality is indispensable, which means that the last phase item of $s_A(\cdot)$ is less $\pi/2$

$$
\frac{4\pi}{\lambda}\frac{V^2 \cos^2(\alpha)}{2r}\left(\frac{T_c}{2}\right)^2 \leq \frac{\pi}{2}
\tag{11}
$$

Eq. (11) is the choosing principle of the coherent processing time in the azimuth direction; the result is the restriction of the integration time in the azimuth direction as follows:

$$
T_c \leq \frac{1}{V\cos(\alpha)}\sqrt{\lambda r} \approx \frac{\sqrt{\lambda r}}{V}
\tag{12}
$$

Then constrain of the number of samples can be computed as follows:

$$Ns \le \frac{PRF \sqrt{\lambda r}}{V} \qquad (13)$$

Due to the parameters of Table 1 , the number of samples must meet $Ns \le 90$ sample in azimuth, satisfying constrained of the coherent summation in azimuth. The number of samples $Ns = 64$ is used here; the resolution during MOCO along azimuth dimension is about 5.4 m (L_{SAR} / Ns), which allows for an accurate accommodation of topography variations.
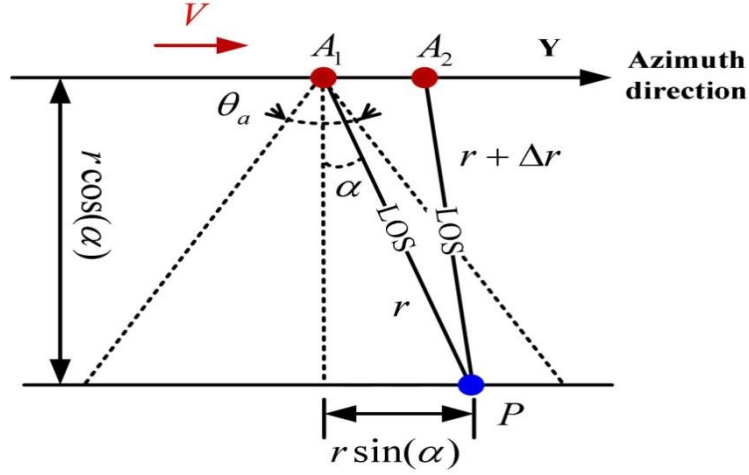

Fig. 3 Analysis of point target echo slant range plane

Fig. 4 shows the block diagram of the proposed algorithm. The idea is that selecting small number of samples Ns along azimuth dimension in time domain, and applying azimuth FFT along that same dimension, allows for a time-frequency (or time-angle) dependent correction. With this principle, the authors of [13-15] were able to apply accurate MOCO to low-frequency wide-beam data. A further step is to apply a topography-dependent correction using the same principle. The topography- and aperture-dependent MOCO, the algorithms rely on the well-known time–frequency relation of the azimuth SAR signal. The mapping between time and frequency is expressed by:

$$f_a(t_a, t_{ao}; r) = \frac{2V}{\lambda} \sin(\beta) = \frac{2V^2}{\lambda} (t_a - t_{ao}) \Big/ \sqrt{r^2 + V^2 (t_a - t_{ao})^2} \qquad (14)$$

where β is the azimuth angle corresponding to an azimuth frequency f_a. The relation between azimuth frequencies and azimuth angles through the beam is given by the Doppler formula

$$\beta(i) = \sin^{-1}(\lambda \cdot f_a(i)/2V) \qquad (15)$$

where i refers to vector location after azimuth FFT, and $f_a(i)$ is the azimuth frequency related to location or scatter i. Eq. (15) means that a certain azimuth frequency corresponds to targets seen from the platform at a certain azimuth angle $\beta(i)$. The conversion between the azimuth angles $\beta(i)$ to azimuth positions $y(i)$ is given by:

$$y(i) = y_{0j} + r \tan\left[\beta(i)\right]$$ (16)

where y_{0j} is the azimuth center position of subaperture i.

Therefore, knowing the azimuth position and depending on a DEM that has be back geocoded to slant-range geometry, it is possible to know all three coordinates in space of the target $P_i(x, y, z)$ and, consequently, to compute the correct range error $\delta R(i)$.

The topography-dependent MOCO algorithm applied after conventional second-order MOCO, because at that stage, range compression has already been applied. Therefore, it is possible to perform the following residual range-dependent phase correction as follows:

$$H(i,r) = \exp\left[j\frac{4\pi}{\lambda}\left(\delta R(i) - \delta R_{ref}(i)\right)\right] = \exp\left[j\frac{4\pi}{\lambda}\delta R_{topo}(i)\right]$$ (17)

where $\delta R(\cdot)$ is the true range error computed by determine scatter position that satisfy azimuth position and close approach range using DEM, $\delta R_{ref}(\cdot)$ is the total MOCO correction already applied to the center of segment j, i.e., first and second-order MOCO corrections, and $\delta R_{topo}(\cdot)$ is the range error due to topographic variation. Notice that Eq. (17) is applied in the range-Doppler domain as depicted in Fig. 4.

After operation of all range in a certain segments, then, the segment is azimuth FFT and stored, before continuing to process the next azimuth segment. After finishing, all segments in azimuth recombine it. Finally, matched filtering as standard stripmap SAR processing is performed the azimuth compression.
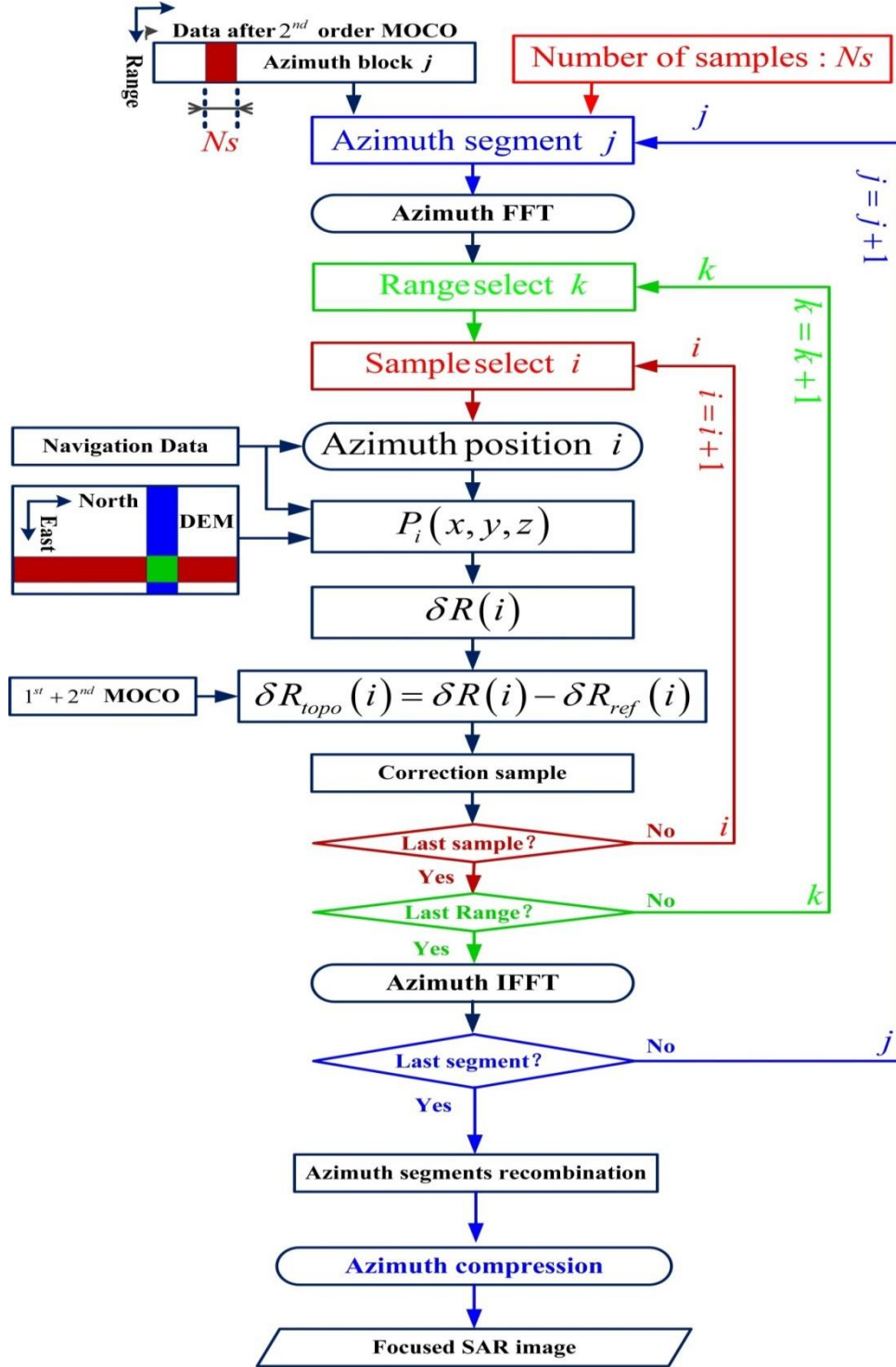
Fig. 4 Block diagram of the topography-dependent MOCO algorithm.

4. Simulation Results

An airborne-SAR simulation data is utilized in this part to validate the topography-Dependent MOCO. The heights or altitudes of scene are change from 375m to 677m. The airborne-SAR parameters are shown in Table 1. The scene area contains five point targets, which help to measure the quality of topography-Dependent MOCO.

Fig. 5 shows the position and velocity in N-frame. The nominal and actual positions in east, north and up are shown in Fig. 5 (a), (c), and (e), respectively. Then the nominal and actual velocities in east, north and up are shown in Fig. 5 (b), (d), and (f), respectively. The invariant range error is shown in Fig. 6(a) and the along-track deviation from nominal path is

shown in Fig. 6(b). In Fig. 7(a) and (b) the topographic variation in scene area in two and three dimension are shown, respectively.

Fig. 8(a) is the focused image without MOCO. Then, the focused images with MOCO based on the navigation data (Case 1) are shown in Fig. 8(b). Finally, the focused images with the topography-dependent motion compensation-with subaperture (Case 2) are shown in Fig. 8(c). The rectangle area for PT1-5 in Fig. 8(b) and (c) are comparison in Fig. 9.
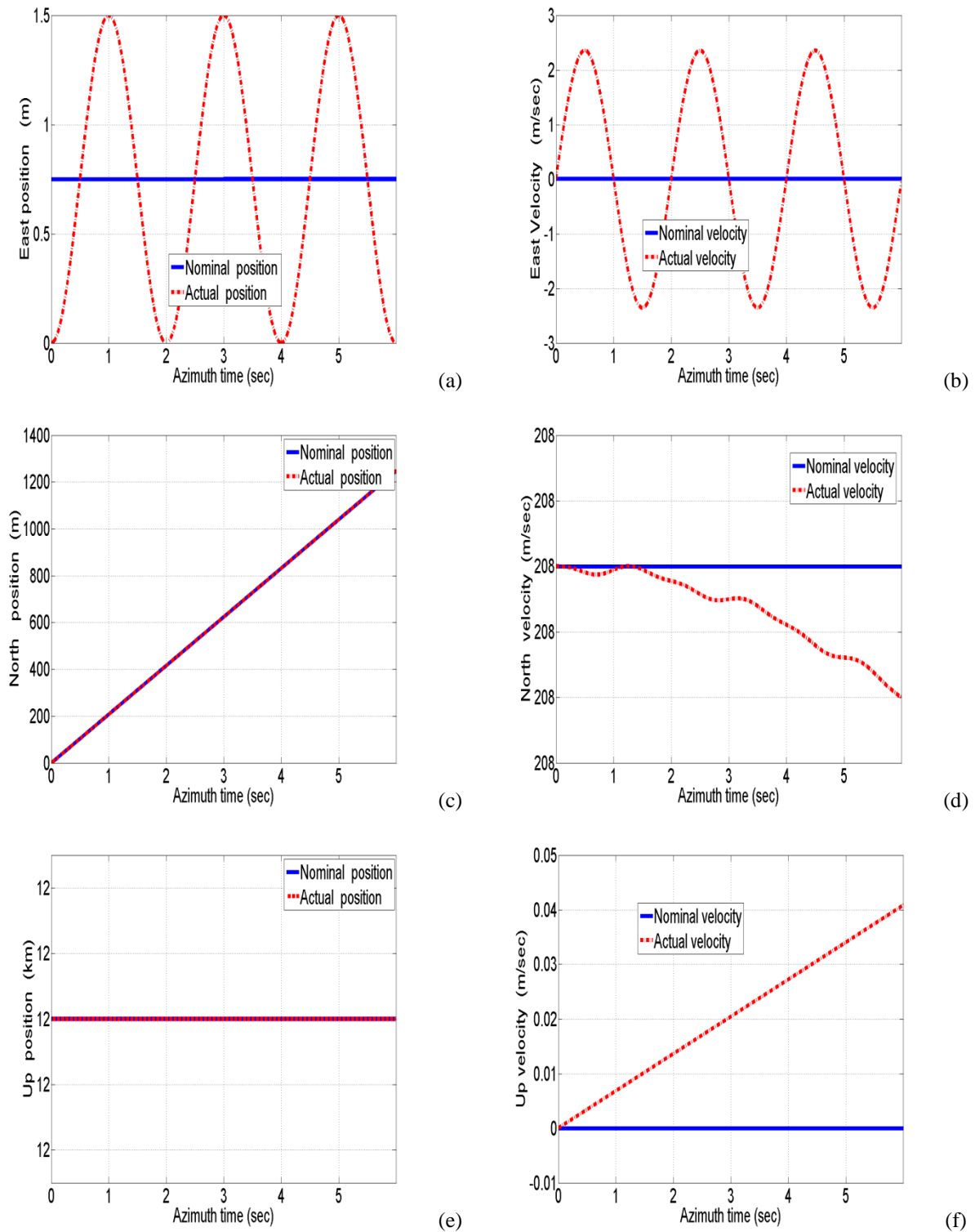

Fig. 5 Nominal and actual for position and velocity. (a) East position. (a) East velocity. (b) North position. (b) North velocity. (b) Up position. (b) Up velocity.
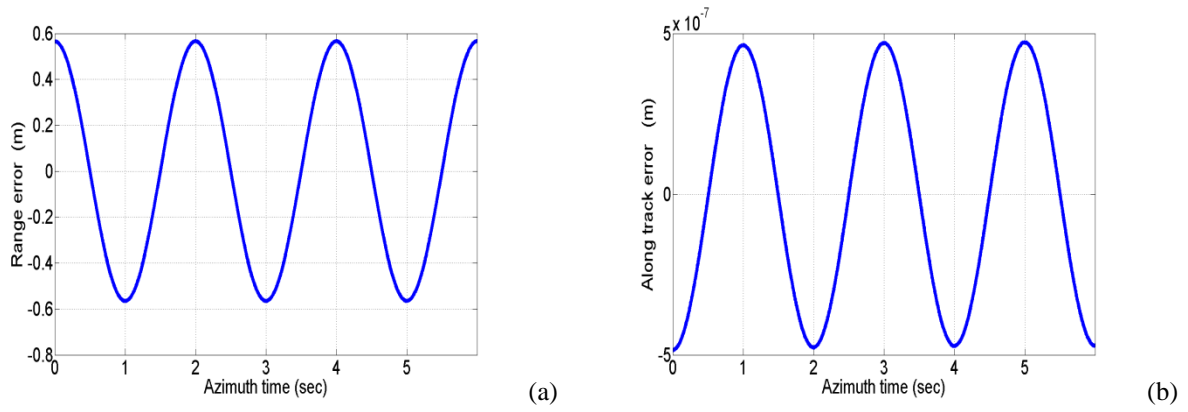
(a)

(b)

Fig. 6 Cross-track and along-track motion errors in real data. (a) Range error. (b) Along-track phase perturbation.
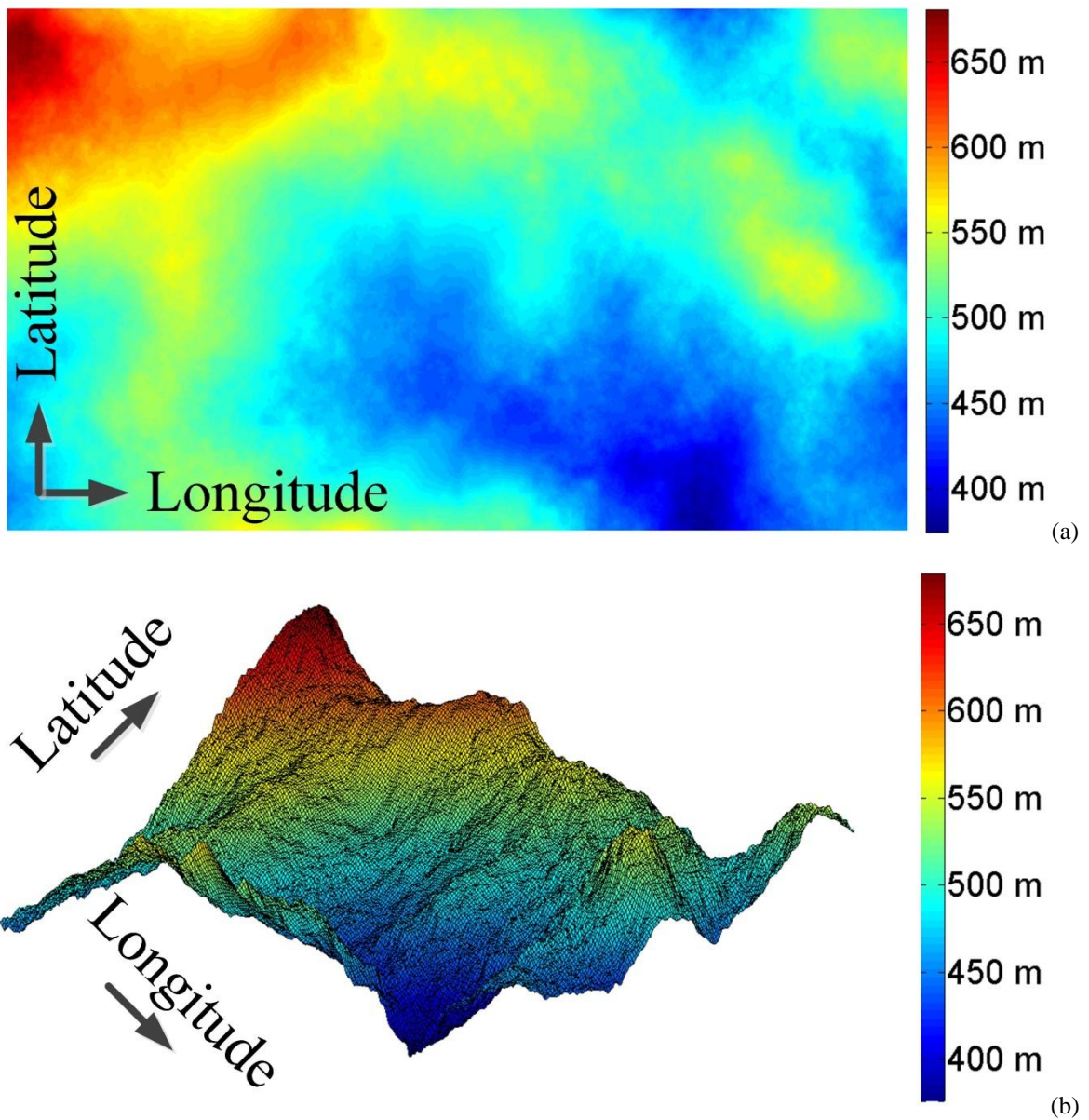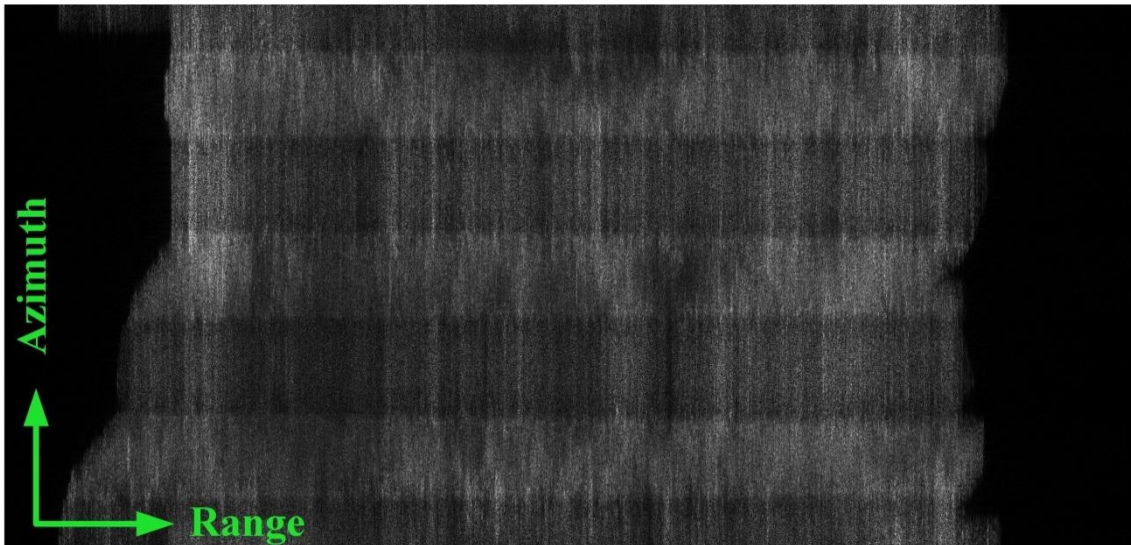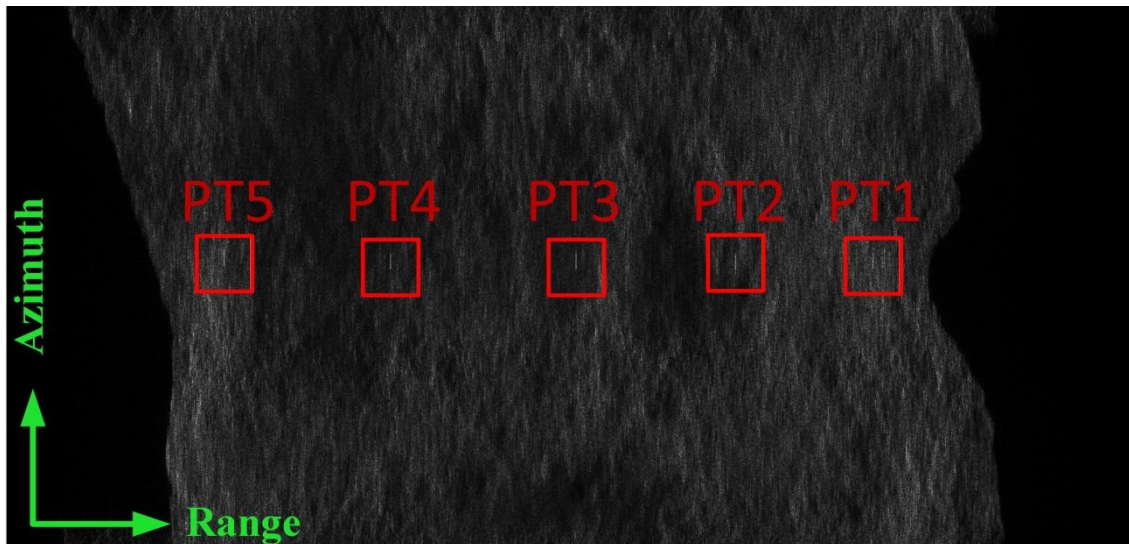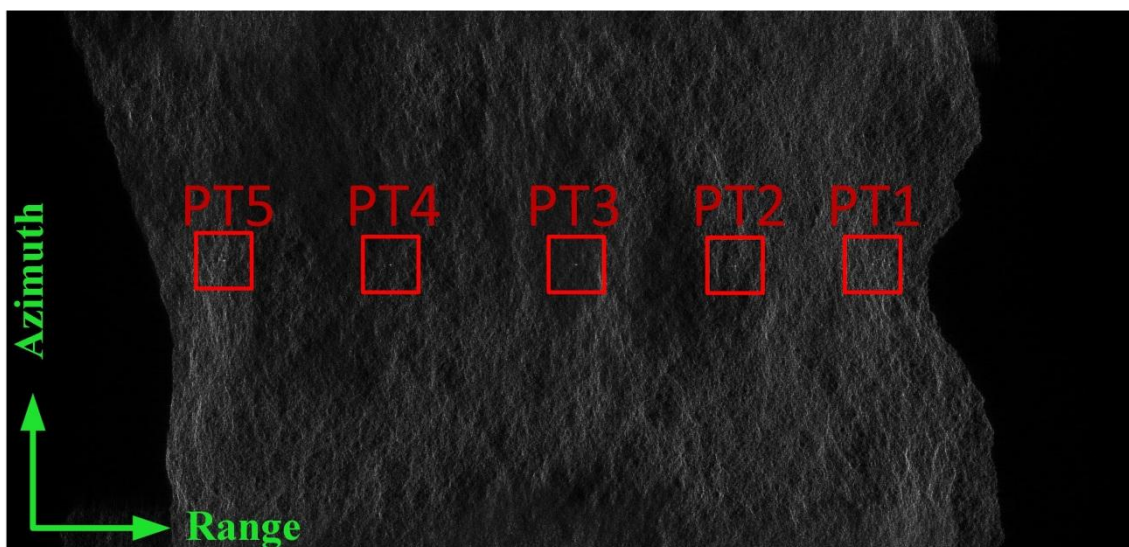

(a)

(b)

Fig. 7 The altitude of scene area. (a) Two dimension. (b) Three dimension.

Fig. 8 The Focused image in different cases. (a) The focused image without MOCO. (b) The focused image with MOCO (Case 1). (c) The foucuse image with the topography-dependent motion compensation-with subaperture (Case 2).
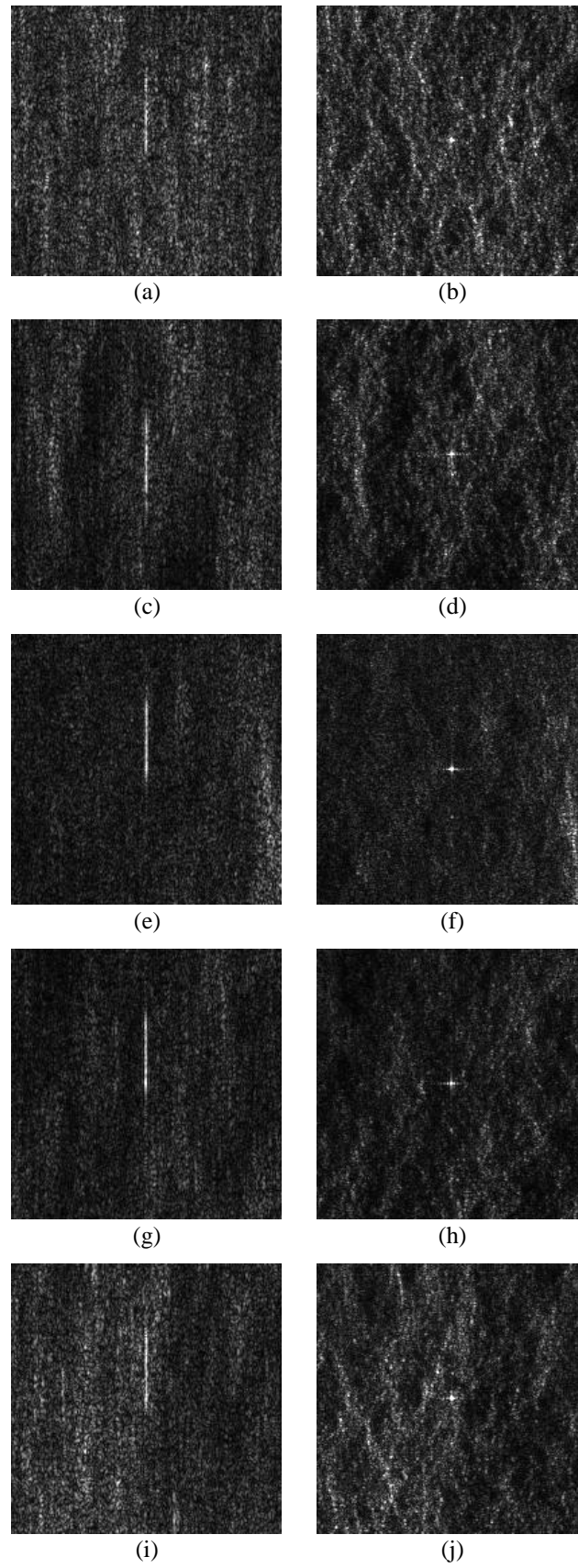
Fig. 9 Foucsed in rectagle area in Fig. 8. (a)PT1 in case 1. (b)PT1 in case2. (c)PT2 in case 1. (d)PT2 in case 2. (e)PT3 in case1. (f)PT3 in case 2. (g)PT4 in case 1. (h)PT4 in case2. (i)PT5 in case 1. (j)PT5 in case 2.
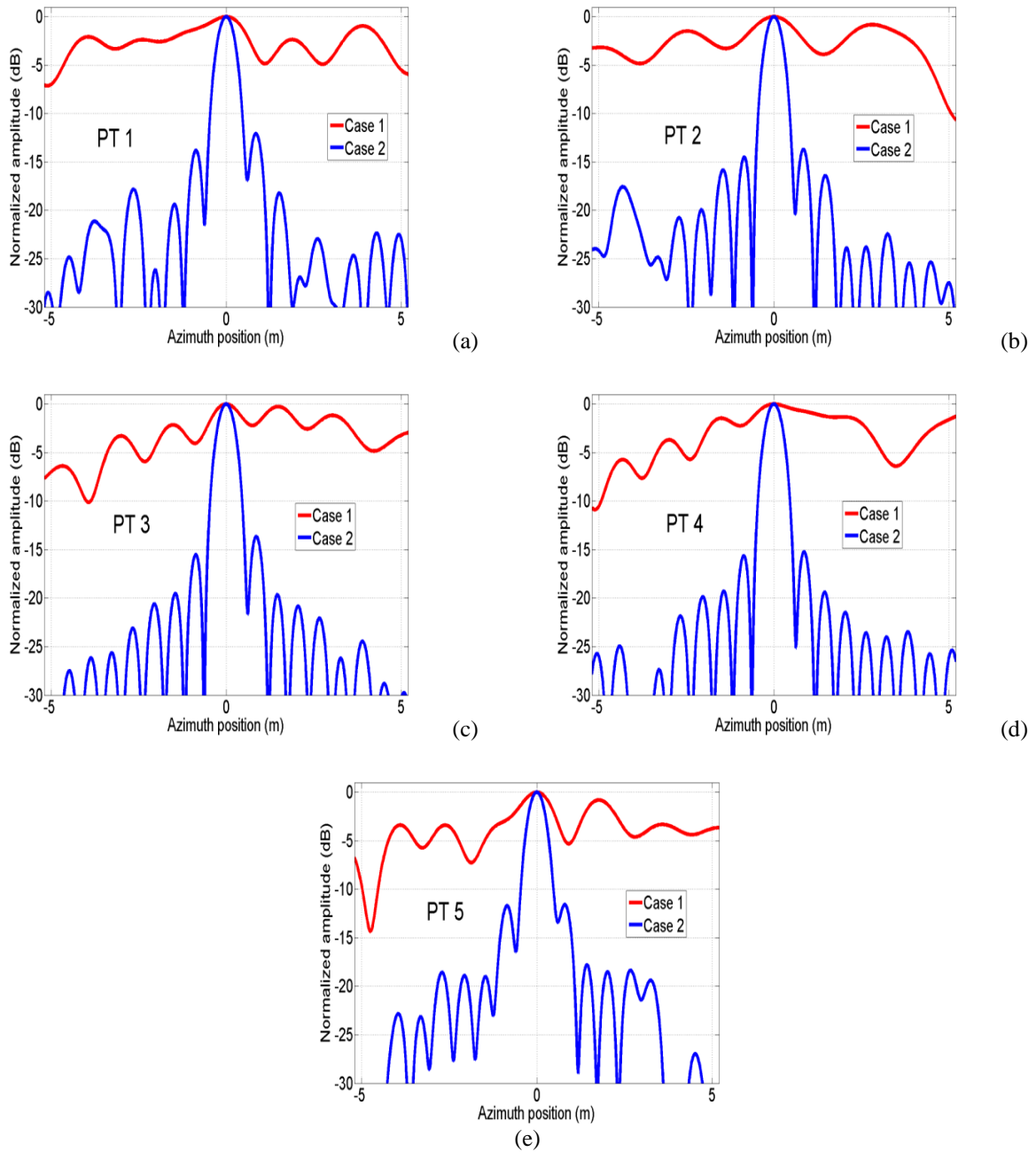
Fig. 10 Amplitude response of PT1-5. (a) PT1. (b) PT2. (c) PT3. (d) PT4. (e) PT5.

Table 2The high power reflector point analysis

		IRW[m]	PSLR[dB]	ISLR[dB]
PT1	Case 1	3.629	-0.9480	2.2419
	Case 2	0.5428	-12.0758	-9.2566
PT2	Case 1	2.1233	-0.8106	3.0523
	Case 2	0.5366	-13.7097	-9.1289
PT3	Case 1	4.2945	-0.2577	5.2835
	Case 2	0.5449	-13.6557	-11.2690
PT4	Case 1	4.6938	-1.4532	1.5943
	Case 2	0.5469	-15.2301	-11.5954
PT5	Case 1	1.5161	-0.8041	2.7302
	Case 2	0.5407	-11.5886	-8.0250

Table 3 Performance comparison

			Sharpness	Entropy	Contrast	Dynamic-range (dB)
Fig. 8		without MOCO	3.2136	16.1712	1.6742	122.9383
		Case1	6.2916	16.1161	1.8008	131.6332
		Case2	42.092	15.8959	15.8959	138.4912
Fig. 9	PT1	Case1	1.4110	11.1770	1.2301	76.7046
		Case2	25.314	10.8533	3.1698	83.3716
	PT2	Case1	5.4331	11.0641	1.5184	66.2890
		Case2	26.816	10.6618	5.9457	85.7173
	PT3	Case1	4.7045	10.9799	1.8273	81.1616
		Case2	28.475	10.6538	8.0850	91.6325
	PT4	Case1	3.7843	11.0248	1.8117	79.0089
		Case2	27.572	10.5189	9.6950	89.7266
	PT5	Case1	1.3046	11.0914	1.4162	71.7318
		Case2	24.988	10.7616	4.2708	81.3056

The focused image and the amplitude responses of PT1-5 are compared in Fig. 9 and Fig. 10 for different cases, respectively. Case1 is the red color plot for MOCO depends on navigation data. Case2 is the blue color plot for the topography-dependent motion compensation-with subaperture. In Fig. 9 and Fig. 10, it is proved that the topography-dependent motion compensation-with subaperture method (case 2) can well compensate the motion error for airborne-SAR due to topographic variation. To make it clearer, The point target analysis for impulse response width (IRW), peak sidelobe ratio (PSLR) and integrated sidelobe ratio (ISLR) measured in azimuth direction of PT1-5 is listed in Table 2.

In Table 2, Fig. 9 and Fig. 10, it can be observed that IRW, PSLR and ISLR of PT1-5 in azimuth direction are improved, and the focusing quality in azimuth for case 2 is largely enhanced in visualization and measurement parameters. In Table 3, it can be observed that the focused image with the topography-dependent motion compensation-with subaperture method (case 2) has the larger image sharpness, higher contrast, bigger dynamic-range, and minimum entropy than the focused image MOCO using navigation data. Therefore, the topography-dependent motion compensation-with subaperture (case 2) is well suitable for the motion compensation of airborne-SARs for topographic variation scene area.

5. Conclusions

The focused image affected by topography variation of scene area. For this reason we should take topography variation of illuminated area in consideration and computed accurate phase error for every point in scene area depend on digital elevation model. The strategy used for compensation topography variation is the aperture-dependent MOCO is discussed. The simulation data shows the validity of the topography-dependent motion compensation with subaperture algorithm and proves to be feasible for airborne-SARs to compensation topography variation.

6. References

[1]   A. Moreira and H. Yonghong, "Airborne SAR processing of highly squinted data using a chirp scaling approach with integrated motion compensation," *Geoscience and Remote Sensing, IEEE Transactions on,* vol. 32, pp. 1029-1040, 1994.

[2]   G. Fornaro, "Trajectory deviations in airborne SAR: analysis and compensation," *Aerospace and Electronic Systems, IEEE Transactions on,* vol. 35, pp. 997-1009, 1999.

[3]   A. Azouz and Z. Li, "Motion compensation for high-resolution automobile-SAR," *International Journal of Remote Sensing,* vol. 35, pp. 4815-4838, 2014/07/03 2014.

[4]   A. A. E. Azouz and Z. Li. (2015, Improved phase gradient autofocus algorithm based on segments of variable lengths and minimum-entropy phase correction. *IET Radar, Sonar & Navigation 9(4),* 467-479. Available: http://digital-library.theiet.org/content/journals/10.1049/iet-rsn.2014.0201

[5]   J.-T. González-Partida, P. Almorox-González, M. Burgos-Garcia, and B.-P. Dorta-Naranjo, "SAR System for UAV Operation with Motion Error Compensation beyond the Resolution Cell," *Sensors,* vol. 8, pp. 3384-3405, 2008.

[6]   D. E. Wahl, P. H. Eichel, D. C. Ghiglia, and C. V. Jakowatz, Jr., "Phase gradient autofocus-a robust tool for high resolution SAR phase correction," *Aerospace and Electronic Systems, IEEE Transactions on,* vol. 30, pp. 827-835, 1994.

[7]   C. Hian Lim and Y. Tat Soon, "Noniterative quality phase-gradient autofocus (QPGA) algorithm for spotlight SAR imagery," *Geoscience and Remote Sensing, IEEE Transactions on,* vol. 36, pp. 1531-1539, 1998.

[8]   Y. Wei, Y. Tat Soon, and B. Zheng, "Weighted least-squares estimation of phase errors for SAR/ISAR autofocus," *Geoscience and Remote Sensing, IEEE Transactions on,* vol. 37, pp. 2487-2494, 1999.

[9]   K. A. C. de Macedo and R. Scheiber, "Precise topography- and aperture-dependent motion compensation for airborne SAR," *Geoscience and Remote Sensing Letters, IEEE,* vol. 2, pp. 172-176, 2005.

[10]   P. Prats, K. A. C. de Macedo, A. Reigber, R. Scheiber, and J. J. Mallorqui, "Comparison of Topography- and Aperture-Dependent Motion Compensation Algorithms for Airborne SAR," *Geoscience and Remote Sensing Letters, IEEE,* vol. 4, pp. 349-353, 2007.

[11]   P. Prats, A. Reigber, and J. J. Mallorqui, "Topography-dependent motion compensation for repeat-pass interferometric SAR systems," *Geoscience and Remote Sensing Letters, IEEE,* vol. 2, pp. 206-210, 2005.

[12]   A. Moreira and H. Yonghong, "Airborne SAR processing of highly squinted data using a chirp scaling approach with integrated motion compensation," *IEEE Transactions on Geoscience and Remote Sensing,* vol. 32, pp. 1029-1040, 1994.

[13]   A. Potsis, A. Reigber, J. Mittermayer, A. Moreira, and N. Uzunoglou, "Sub-aperture algorithm for motion compensation improvement in wide-beam SAR data processing," *Electronics Letters,* vol. 37, pp. 1405-1407, Nov 8 2001.

[14]   K. A. C. deMacedo and R. Scheiber, "Precise Topography- and Aperture-Dependent Motion Compensation for Airborne SAR," *IEEE Geoscience and Remote Sensing Letters,* vol. 2, pp. 172-176, 2005.

[15]   P. Prats, A. Reigber, and J. J. Mallorqui, "Topography-dependent motion compensation for repeat-pass interferometric SAR systems," *Ieee Geoscience and Remote Sensing Letters,* vol. 2, pp. 206-210, Apr 2005.